A&A 474, 633–637 (2007)
DOI: 10.1051/0004-6361:20078110

Astronomy & Astrophysics

Photospheric magnetic evolution of super active regions⋆

P. Romano[1] and F. Zuccarello[2]

[1] INAF – Osservatorio Astrofisico di Catania, via S. Sofia 78, 95123 Catania, Italy
e-mail: prom@oact.inaf.it
[2] Dipartimento di Fisica e Astronomia – Sezione Astrofisica, Università di Catania, via S. Sofia 78, 95123 Catania, Italy

Received 18 June 2007 / Accepted 11 August 2007

ABSTRACT

Context. Solar flares are one of the most interesting phenomena of solar activity. Although many authors agree that their energy release is related to magnetic reconnection, the phases preceding the magnetic reconnection process are still unclear in several respects.
Aims. We studied the magnetic flux evolution in 26 super active regions observed on the solar disc from Jan. 1, 2000 to Dec. 31, 2006, in order to determine a physical relationship between flares and some properties of the photospheric magnetic fields.
Methods. This analysis is based on full disc line of sight MDI magnetograms. We measured the total magnetic flux, the magnetic flux imbalance, the horizontal magnetic gradient and the number of magnetic features characterized by a collection of pixels lying in the same bins of absolute strength. We also elaborated an algorithm for the identification and the length measurement of the magnetic inversion lines.
Results. We found a correlation between the evolution of the analyzed parameters and the flare occurrence. The most intense phases of activity are associated with phases of emergence of a magnetic field in 15 super active regions and with phases of flux cancellation in 5 super active regions.
Conclusions. Super active regions may be characterized by a different behavior depending on their morphology. Some of them show a continuous flare activity, while others present an alternation of active and quiet phases. The deviations from magnetic polarity balance and the length of the inversion lines characterized by a horizontal magnetic gradient greater than 0.3 G km^{-1} seem to have a major role in producing a magnetic field topology able to trigger flares.

Key words. Sun: activity – Sun: flares – Sun: magnetic fields

1. Introduction

Solar flares are explosive energy release events involving all the layers of the solar atmosphere and cover the entire electromagnetic spectrum and several energy scales. They range from nanoflares with typical energy of about 10^{23} erg to the most energetic events of about 10^{33} erg. In recent decades several authors have agreed that flares might be caused by instabilities of the magnetic field configuration which evolves into a more stable state by reconnecting and changing the topology (see Priest & Forbes 2000, for more details). In particular, the theory of magnetic reconnection in 2D and 3D indicates that reconnection occurs along dynamic boundaries with a thickness of the order of tens of meters, where the magnetic field is characterized by different directions on both sides. Therefore, these magnetic field discontinuities, called current sheets or separators, represent the regions of more interest to study flares, although due to the insufficient resolution of the actual instruments it is not possible to directly observe their formation and the reconnection processes.

The preferential sites for flare occurrence are active regions where the magnetic field emerging from the convection zone is more concentrated. More intense magnetic field together with a more complex topology are usually associated with the most energetic flares. Although many efforts have been made to forecast flare events, at the moment it is not clear what driver mechanism is that is able to induce the unstable configuration of the magnetic field.

Flare models indicate that when a new magnetic flux system is pushed towards a pre-existing, old magnetic flux system, and/or a new emerging flux region pushes through the chromosphere upwards into a pre-existing coronal magnetic field, a current sheet is formed and reconnection can take place.

In order to understand the mechanisms responsible for the storage of the energy delivered during flare events, the relationships between flares and several photospheric magnetic properties have been studied. Many authors have considered the evolution of several parameters during the preflare phase: emergence of new magnetic flux (Nitta et al. 1996), magnetic shear (Sakurai et al. 1992), flux imbalance (Wang et al. 2002), effective distance (Guo et al. 2006), flux of magnetic helicity (see Demoulin 2006, and references therein), length of neutral lines and singular points in the potential field (Cui et al. 2006), electric currents (Zhang 2001), etc. However, these studies did not give a definitive method to predict the flare occurrence.

Recently, Wang et al. (2006) studied five super active regions considering the magnetic gradient derived from line of sight magnetograms and the magnetic shear derived from vector magnetograms. They found a strong correlation between these two quantities along the neutral lines in the active regions and a spatial correlation between the location of the flare ribbons at 1600 Å and the neutral lines where the horizontal magnetic gradient was maximum.

In this context, we tried to find further observational evidence of the correlation between solar flare productivity and some properties of the photospheric magnetic field in 26 super active regions observed from Jan. 1, 2000 to Dec. 31, 2006.

⋆ Tables A.1–A.3 and Figs. B.1–B.9 are only available in electronic form at http://www.aanda.org

These regions, due to their prolific flare activity, can be considered a good target to study the characteristics associated with flare triggering. In particular, we analyse of the magnetic inversion lines characterized by a strong magnetic gradient.

The layout of the present paper is as follows: in the next section we present the data. In Sect. 3 we describe the considered parameters and the methods to compute them. In Sect. 4 we give our results and in Sect. 5 our conclusions.

2. Observations

Solar flare are conventionally classified according to their output of X-ray energy flux in the wavelength range 1 to 8 Å at the peak of their burst. Each class: A, B, C, M or X, corresponds to a peak flux ten times greater than the preceding one, with X class flares having a peak flux of the order of 10^{-1} erg cm^{-2} s^{-1}. Each letter is preceded by a coefficient which represents the multiply factor of the magnitude.

In this work we considered flare events with a peak flux greater than 10^{-4} erg cm^{-2} s^{-1} registered by GOES and described in the reports of the Space Environment Center over 6 years, from Jan. 1, 2000 to Dec. 31, 2006. During this period the GOES satellite recorded 16 358 events. For 10 080 flares it was possible to identify the active regions where these events occurred. In this way we selected 1037 active regions where at least one flare occurred. In order to measure the flare activity in each region and its evolution, we defined, according to Li et al. (2004), a Flare Index $I(t)$ at the time t as:

$$I(t) = 0.1 \times \sum B(t) + \sum C(t) + 10 \times \sum M(t) + 100 \times \sum X(t) \quad (1)$$

where $B(t)$, $C(t)$, $M(t)$ and $X(t)$ are the coefficients of the flare that occurred at the time t and belonging to the class B, C, M and X, respectively.

In Table A.1 of Appendix A we report the distribution of the maximum of the Flare Index reached by each active region. We singled out 910 active regions with a maximum of the Flare Index between 0 and 100. We can consider these active regions as characterized by a low flare activity. As the level of activity increases, the number of active regions decreases. We can distinguish 101 active regions characterized by a Flare Index between 100 and 500. In the tail of the distribution, there are 26 active regions that reached a Flare Index greater than 500. We concentrated on these regions, which we called *super active regions*, due to the particularly intense flare activity during their passage over the solar disc (see Table A.2 in Appendix A).

We used MDI/SOHO full-disc observations at Ni I 6767.8 Å, which provide the line-of-sight component of the magnetic field. For each super active region we considered the magnetograms taken during the time interval between the first and the last flare, with a time resolution of 96 min. Each magnetogram consists of 1024×1024 pixels with a plate scale of 1.98 arcsec pixel^{-1}. We analyzed a sub-field centered on each active region such that the maximum magnetic flux imbalance was less than 20%. We neglected all the magnetograms where the longitudinal angular distance of the super active region from the disk center was greater than 41 degrees.

3. Data analysis

For each super active region we computed several parameters from the selected line-of sight magnetograms. First we derived the total magnetic flux:

$$|\Phi|_{\rm tot} = |\Phi_+| + |\Phi_-| \quad (2)$$

and the magnetic flux imbalance:

$$|\Phi|_{\rm tot} = |\Phi_+| - |\Phi_-| \quad (3)$$

where $|\Phi_+|$ and $|\Phi_-|$ are the absolute values of the magnetic flux for the positive and negative polarities, respectively. In the determination of these two parameters we corrected the magnetograms for the angle between the magnetic field direction and the observer's line of sight, for the foreshortening of the active region with the distance from central meridian passage (Wood & Martens 2003) and for the underestimation of the flux density following the results of Berger & Lites (2003). Moreover, we considered only the magnetogram pixels with an absolute value $|B_z| \geq 300$ G, in order to neglect the contribution of the network inside the selected sub-field.

The longitudinal magnetograms were also used to derive the magnetic field gradient maps. The photospheric field gradients have long been known to be related to flaring activity (Zhang et al. 1994). In particular, Zhang (2001) found that the shear and the gradient of the magnetic field are important in defining the non-potentiality of the active regions and they reflect the strength of the electric current in the region. We focus on the magnitude of the horizontal gradient of the line of sight field, which can be calculated by:

$$|\nabla B_z| = \left[\left(\frac{\partial B_z}{\partial x} \right)^2 + \left(\frac{\partial B_z}{\partial y} \right)^2 \right]^{1/2} . \quad (4)$$

In the determination of this quantity we considered all the values of the magnetic field flux from the minimum value recorded.

We also elaborated an algorithm to characterize the areas of major interest around the inversion lines of the line-of-sight magnetograms. They represent the photospheric manifestation of the separatrix surfaces which separate different dipolar domains, where the reconnection processes can take place.

We can divide the algorithm into three steps. In the first step we set to zero the pixels characterized by a magnetic field between –300 and 300 G (Fig. 1a) and we binarized the remaining pixels in +1 and –1 for positive and negative fields, respectively (Fig. 1b). In the second step we considered a sliding window of 5×5 pixels and selected only the pixels in the center of the window having at least one 24-neighbour with the opposite sign. We set to zero the unselected pixels. In this way we selected the pixels of positive and negative polarities along the inversion lines (Fig. 1c). The last step allowed us to select only the inversion lines characterized by a particular intense magnetic horizontal gradient, i.e. the lines of major interest for the interaction between oppositely directed magnetic fields. We excluded the lines where the horizontal gradient was less than 0.3 G km^{-1} (Fig. 1d). Although Severny (1960) gave a threshold value of about 0.1 G km^{-1} as a preflare condition, we fixed this higher threshold in order to neglect the lines of minor interest. Then we computed the length l of these lines and the maximum horizontal gradient of the magnetic field $(\nabla_{\rm h} B_z)_{\rm max}$ along them.

Finally, we took into account the number $N_{\rm s}$ of magnetic features characterized by a magnetic field greater than 1500 G and by a minimum size of 10 pixels ($\sim$7250 km^2). We identified these features grouping collections of pixels lying on the same peaks in absolute field strength. This grouping is accomplished by the software YAFTA (Welsh & Longcope 2003). $N_{\rm s}$ provided useful information about the formation, disappearance, merging and fragmentation of the magnetic features during the active region evolution.

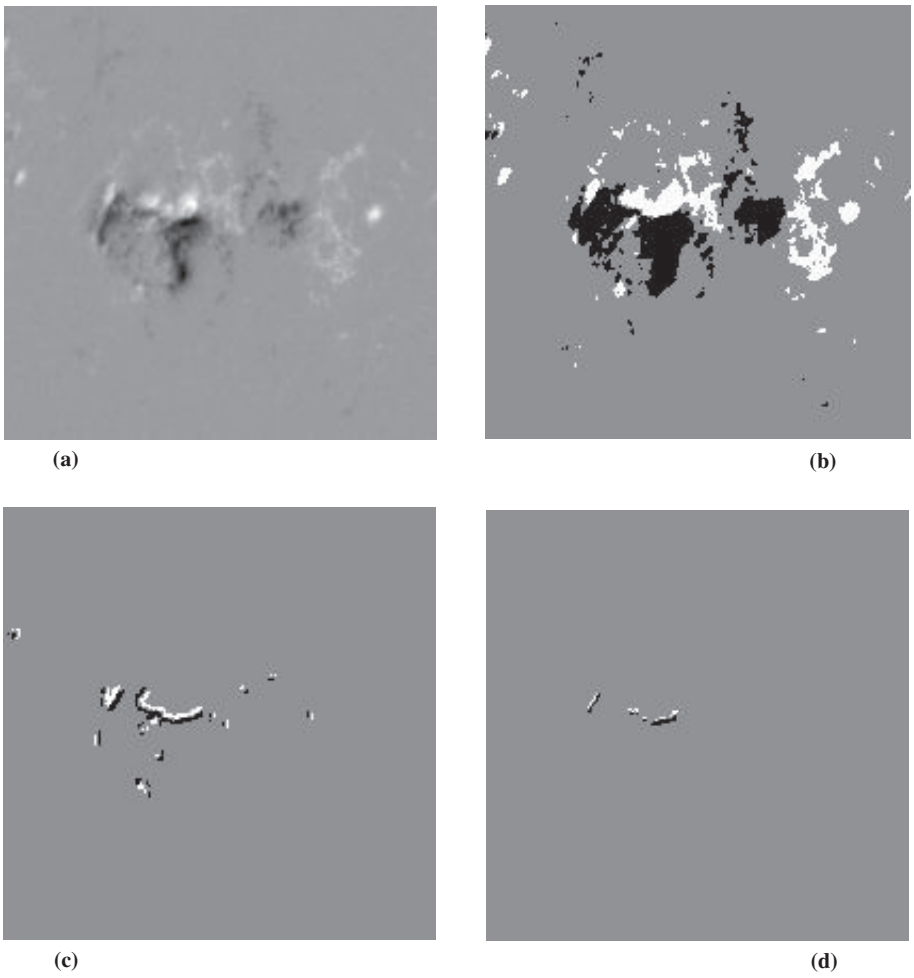

Fig. 1. Algorithm application on a magnetogram of the active region NOAA 9077. **a)** Magnetic field between –300 and 300 G. **b)** Binarized magnetogram. **c)** Map of the pixels of positive and negative polarities along the inversion lines. **d)** Inversion lines of major interest where the horizontal gradient was greater than 0.3 G km^{-1}.

4. Results

We report in Fig. 2 the evolution of the total magnetic flux $\Phi_{\rm tot}$, flare activity, magnetic flux imbalance $\Phi_{\rm imb}$, length of inversion lines l, maximum horizontal gradient $(\nabla_{\rm h} B_z)_{\rm max}$ and number of magnetic features $N_{\rm s}$ for NOAA 10375 as an example. Similar behavior is shown by most of the super active regions (see Appendix B for the other plots).

In order to describe the variations of regime of flare activity in an active region during its passage across the solar disc, we represented each single flare with a black bar whose height is proportional to the X-ray flare peak, and the total of the Flare Index over 50 h with grey bars. $t = 0$ corresponds to the time when the first flare was registered. We used the logarithmic scale to show the magnitude of different flares in the same plot.

Looking at the Flare Index we note that each active region shows a different evolution: most of them present one or more peaks of activity during their passage across the solar disc. Only 2 active regions (NOAA 10069 and NOAA 10488) show a continuous increase of their flare activity and another 2 regions (NOAA 9690 and NOAA 10808) show a continuous decay of activity. However, apart from their evolution, most of the regions show a strong correlation between the variations of flare activity and the computed quantities: the behavior of the grey bars are well reproduced by the behavior of most of the studied parameters. The most evident correlation seems to exist between the length of the neutral lines and the flare activity. The phases of increase and decrease of flare occurrence always correspond to the l increase and decrease, respectively.

To demonstrate these correlations we computed the Spearman correlation coefficient for each parameter q and the Flare Index I:

$$r_q = \frac{\sum_{i=0}^{N-1}(q_i - \bar{q})(I_i - \bar{I})}{\sqrt{\sum_{i=0}^{N-1}(q_i - \bar{q})}\sqrt{\sum_{i=0}^{N-1}(I_i - \bar{I})}} \quad (5)$$

where N is the number of analyzed magnetograms, q_i and I_i are the parameter value and Flare Index corresponding to the time of the $i_{\rm th}$ magnetogram (see Table A.3 in Appendix A).

Only 6 super active regions do not show any correlation of the flare activity with the total magnetic flux, while 15 super active regions show a positive correlation and 5 an anticorrelation. In particular, the peaks of activity of 57.7% of the regions are associated with the emergence of new magnetic flux and the peaks of activity of 19.2% of the regions are associated with the cancellation of the photospheric magnetic field.

In 88.4% of the regions the magnetic flux imbalance also shows a good correlation with the flare activity. In many cases the increase of $\Phi_{\rm imb}$ in absolute value corresponds to a phase in which, although the intensity of the flare remains modest, the number of flares increases.

The horizontal gradient of the magnetic field is very high in this kind of region, compared with those showing a lower flare activity, but we do not see any particular variation of the maximum of $\nabla_{\rm h} B_z$. In most of the regions its value changes by tenths of G km^{-1}. Only in half of the selected targets do we note a consistent variation of $(\nabla_{\rm h} B_z)_{\rm max}$ with the Flare Index.

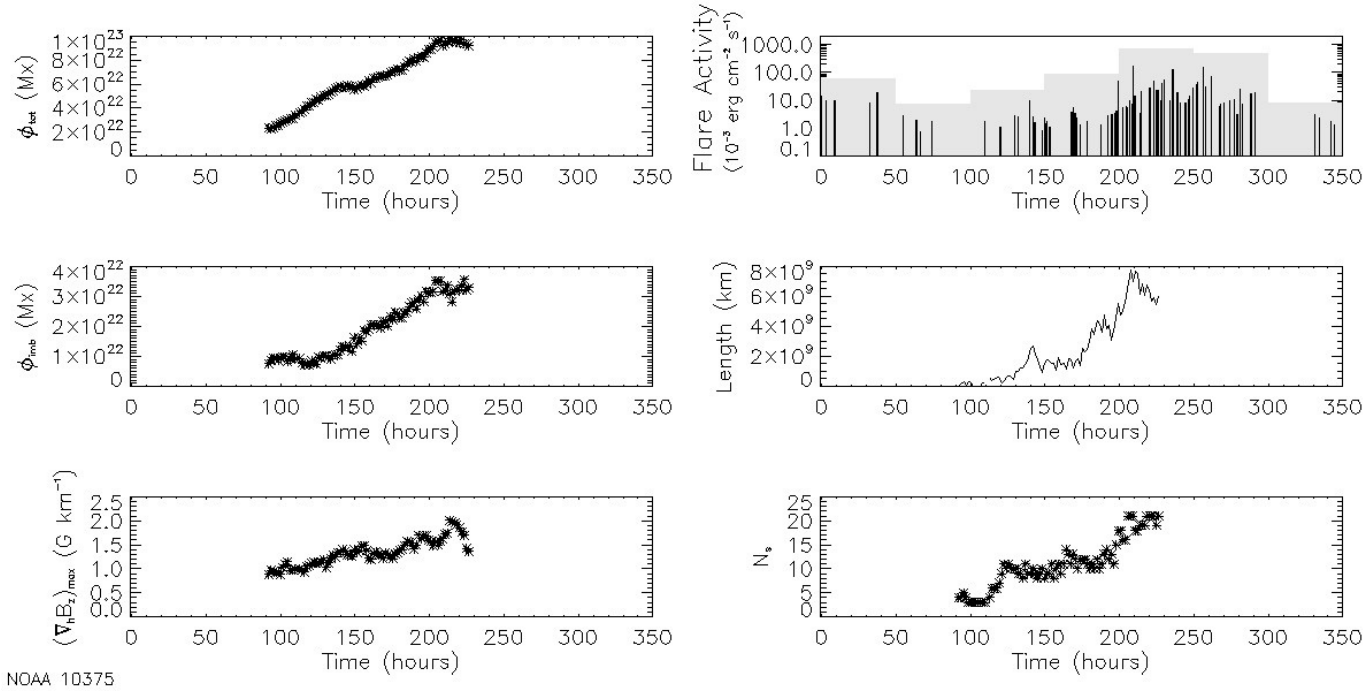

Fig. 2. Φ_{tot}, flare activity, Φ_{imb}, l, $(\nabla_h B_z)_{max}$ and N_s vs. time for NOAA 10375.

The strong correlation between the length of the neutral lines characterized by a magnetic gradient greater than 0.3 G km^{-1} and the level of flare activity is confirmed by the high values of the correlation coefficients in almost all super active regions (about 73%)

Finally, the values of r_{N_s} show that N_s is well correlated with the Flare Index for 20 super active regions.

5. Discussion and conclusions

This study investgates the possible correlation between the magnetic evolution at the photospheric level and the flare activity in active regions, characterized by a particularly frequent and intense energy release. We selected 26 super active regions during half of the 23th solar cycle (6 years). From the line-of-sight magnetograms taken by MDI, we deduced that these regions are characterized by a total magnetic flux between 5×10^{21} and 5×10^{22} Mx. In many cases the peak of the magnetic flux measured at the photospheric level matches with the peak of flare activity. This means that the magnetic concentration is a first condition to produce an increase of activity.

This study shows that the evolution of the magnetic flux imbalance seems to closely follow the frequency of the observed events: the greater the imbalance in absolute value, the greater the number of events registered in the same time interval. Green et al. (2003) excluded that the non-linear response of MDI is the source of the lack of balance between opposite polarity and they saw that polarity imbalance is associated with some flares, but also that imbalances of similar magnitude occurred outside flare or CME times. Therefore, they concluded that flares and CMEs are not closely related to the observed changes in magnetic polarity balance. However our results seem to confirm the result of Wang et al. (2002), who found that in 6 active regions deviations from polarity balance associated with flares were permanent.

Although the magnetic field gradient has long been known to be related to flaring activity (Zhang et al. 1994), in the super active regions examined, the maximum of the photospheric field gradient does not show any particular variation. On the contrary, the horizontal magnetic gradient along the inversion lines allowed us to identify the portions of magnetic discontinuities whose length seem to be correlated with the flare occurrence. 73% of the super active regions shows a strong correlation between l and I. Due to the low time resolution of the MDI magnetograms, we could not establish whether the increase of l occurs before or after the flares. However, we think that this method allows us to identify the areas along the inversion lines where the current sheets perpendicular to the solar surface are formed and where the reconnection processes can take place. Therefore, as l increases, the flare occurrence probability increases. One of the advantages of this parameter is that we restrict our analysis to the edges of the magnetic structure and therefore we can neglect the presence of saturation in the MDI magnetograms.

We also found that the number of magnetic features characterized by a magnetic field greater than 1500 G and by a minimum size of 10 pixels (~7250 km^2) is another useful parameter for the description of the evolution of flare activity. In 17 of 26 active regions the number of the identified features increased with increasing activity. This parameter gives us information about the formation of new consistent magnetic concentrations, which could be important for flare triggering. Taking into account the model of Heyvaerts et al. (1977), an increase of the structures at photospheric level provides a greater probability of the interaction between a preexisting flux tube and a new emerging one.

Therefore, we conclude that the total magnetic flux, the polarity imbalance, the length of the inversion line and the number of features can be useful in determining the variation of the rate and intensity of flares in particularly prolific active regions.

At the moment the lack of polarimetric studies with sufficient time resolution and good temporal coverage does not allow us to investigate the correlation between flare activity and other parameters depending on all three components of the magnetic field. We believe that Solar B with its vector magnetograms will provide a more useful tool to study the magnetic field

evolution of super active regions and to find different algorithm in order to describe their morphology and photospheric properties. Moreover, the extension of this work to active regions of lower flare activity could provide further evidence of the importance of these parameters in the study of the condition leading to flare trigger, over a more statistically significant sample.

Acknowledgements. The authors wish to thank the team of MDI instrument on board of SOHO. This work was supported in part by the Italian Ministry of Education, University and Research, in part by the Istituto Nazionale di Astrofisica (INAF), in part by the Agenzia Spaziale Italiana (contract I/035/0 ASI/INAF-OATO), in part by the Università degli Studi di Catania and in part by th European Commission trough the SOLAIRE Network (MTRN-CT-2006-035484).

References

Berger, T. E., & Lites, B. W. 2003, Sol. Phys., 213, 213
Cui, Y., Li, R., Zhang, L., He, Y., & Wang, H. 2006, Sol. Phys., 237, 45
Demoulin, P. 2006, cosp, 36, 117D
Green, L. M., Demoulin, P., Mandrini, C. H., & Van Driel-Gesztelyi, L. 2003, Sol. Phys., 215, 307
Guo, J., Zhang, H., Chumak, O. V., & Liu, Y. 2006, Sol. Phys., 237, 25
Heyvaerts, J., Priest, E. R., & Rust, D. M. 1977, ApJ, 216, 123
Leka, K. D., Fan, Y., & Barnes, G. 2005, ApJ, 626, 1091
Li, Y., Luhmann, J., Fisher, G., & Welsch, B. 2004, J. Atm. Solar-Terrestrial Phys., 66, 1261
Michard, R. 1971, IAU Symp., 43, 259
Nitta, N., van Driel-Gesztelyi, L., Leka, K. D., & Shibata, K. 1996, Adv. Space Res., 17, 201
November, L. J., & Simon, G. W. 1988, ApJ, 333, 427
Priest, E. R., & Forbes, T. 2000, Magnetic Reconnection - MHD Theory and Applications (Cambridge: Cambridge University Press)
Priest, E. R., Hood, A. W., & Anzer, U. 1989, ApJ, 344, 1010
Rust, D. M., & Kumar, A. 1994, Sol. Phys., 155, 69
Sakurai, T., Shibata, K., Ichimoto, K., Tsuneta, S., & Acton, L. W. 1992, Publ. Astron. Soc. Jpn., 44, 123
Severny, A. B. 1960, Izv. Krymsk. Astrofiz. Obs., 22, 12
van Ballegooijen, A. A., & Martens, P. C. H. 1989, ApJ, 343, 971
Wang, H., Spinoch, T. J., Qiu, J., et al. 2002, ApJ, 576, 497
Wang, H. M., Song, H., Jing, J., et al. 2006, Chin. J. Astron. Astrophys., 6, 4, 477
Welsch, B. T., & Longcope, D. W. 2003, ApJ, 588, 620
Wood, P., & Martens, P. 2003, Sol. Phys., 218, 123
Zhang, H. 2001, ApJ, 557, L71
Zhang, H., Ai, G., Yan, X., Li, W., & Liu, Y. 1994, ApJ, 423, 828

Online Material

Appendix A: Tables

In Table A.1 we report the distribution of the maximum of the Flare Index reached by each super active region.

Table A.1. Distribution of the maximum of the Flare Index reached by the active regions from Jan. 1, 2000 to Dec. 31, 2006.

Flare Index Range	No of ARs.
0–100	910
100–200	54
200–300	30
300–400	10
400–500	7
500–600	4
600–700	3
700–800	2
800–900	2
900–1000	2
1000–1100	2
1100–1200	2
1200–1300	1
1300–1400	4
1400–2300	0
2300–2400	3
2400–4800	0
4800–4900	1

We studied the photospheric magnetic evolution of 26 active regions which reached a Flare Index greater than 500. We report the name of these regions in the first column of Table A.2. In the second and third columns of Table A.2 we report the time of the first and the last flare, produced by each of them. The number of magnetograms analysed for each active region is reported in the fourth column.

In Table A.3 we report the correlation coefficients for each quantity and for each active region. We put in italic face the values of the correlation coefficients when the probability that the two quantities are correlated is less than 90%.

Appendix B: Parameter evolution

In Figs. B.1–B.9 we report the evolution of the total magnetic flux $\Phi_{\rm tot}$, flare activity, magnetic flux imbalance $\Phi_{\rm imb}$, length of inversion lines l, maximum horizontal gradient $(\nabla_{\rm h} B_z)_{\rm max}$ and number of magnetic features $N_{\rm s}$ for each of the 26 super active regions.

Table A.2. Super active regions from Jan. 1, 2000 to Dec. 31, 2006.

NOAA	First Flare	Last Flare	No of Magn.
9026	Jun. 1, 2000 01:01 UT	Jun. 10, 2000 17:19 UT	90
9077	Jul. 9, 2000 02:43 UT	Jul. 19, 2000 16:21 UT	71
9236	Nov. 22, 2000 04:59 UT	Nov. 27, 2000 00:21 UT	80
9393	Mar. 24, 2001 09:14 UT	Apr. 4, 2001 06:47 UT	74
9415	Apr. 3, 2001 04:55 UT	Apr. 16, 2001 07:12 UT	87
9433	Apr. 19, 2001 04:52 UT	May. 1, 2001 19:45 UT	65
9591	Aug. 22, 2001 15:10 UT	Sept. 2, 2001 18:06 UT	77
9690	Nov. 6, 2001 08:34 UT	Nov. 15, 2001 17:29 UT	83
9733	Dec. 8, 2001 02:56 UT	Dec. 19, 2001 01:24 UT	89
10030	Jul. 10, 2002 01:56 UT	Jul. 20, 2002 12:44 UT	99
10039	Jul. 23, 2002 00:47 UT	Aug. 3, 2002 19:11 UT	77
10069	Aug. 11, 2002 14:20 UT	Aug. 24, 2002 01:31 UT	84
10314	Mar. 15, 2003 03:44 UT	Mar. 22, 2003 23:03 UT	57
10365	May. 25, 2003 20:38 UT	Jun. 2, 2003 16:01 UT	81
10375	Jun. 1, 2003 04:00 UT	Jun. 15, 2003 12:35 UT	84
10484	Oct. 18, 2003 04:22 UT	Oct. 28, 2003 05:14 UT	93
10486	Oct. 22, 2003 05:21 UT	Nov. 5, 2003 10:56 UT	64
10488	Oct. 27, 2003 14:21 UT	Nov. 4, 2003 10:33 UT	68
10649	Jul. 12, 2004 13:12 UT	Jul. 24, 2004 01:16 UT	88
10652	Jul. 17, 2004 03:49 UT	Jul. 31, 2004 11:49 UT	95
10656	Aug. 6, 2004 23:01 UT	Aug. 19, 2004 14:16 UT	83
10696	Nov. 2, 2004 16:42 UT	Nov. 11, 2004 16:02 UT	92
10720	Jan. 11, 2005 20:46 UT	Jan. 23, 2005 05:23 UT	85
10786	Jul. 1, 2005 05:07 UT	Jul. 15, 2005 17:15 UT	92
10808	Sept. 7, 2005 18:03 UT	Sept. 18, 2005 00:17 UT	52
10930	Dec. 4, 2006 16:01 UT	Dec. 18, 2006 10:37 UT	77

Table A.3. Correlation coefficients for each quantity and for each super active region

NOAA	$r_{\phi_{\rm tot}}$	$r_{\phi_{\rm imb}}$	$r_{(\nabla_{\rm h} B_{\rm z})_{\rm max}}$	$r_{\rm l}$	$r_{N_{\rm s}}$
9026	0.909665	0.190300	0.815089	0.758148	0.826358
9077	0.824289	–0.472078	0.660565	0.672426	0.550992
9236	0.899870	0.786368	*–0.331489*	0.901385	0.700821
9393	0.651950	*0.113192*	*–0.142299*	0.456530	0.462840
9415	–0.292566	*–0.021760*	–0.258807	0.320336	0.195354
9433	0.612297	–0.223606	0.345767	*–0.014616*	0.403159
9591	*–0.136914*	0.716313	0.432169	0.221499	0.866203
9690	–0.334784	0.641709	*0.0173453*	0.922442	*0.112254*
9733	–0.230806	–0.672761	0.434485	*–0.0632346*	*0.029976*
10030	0.183916	–0.261003	0.678190	0.451705	0.483106
10039	*0.134547*	0.37298	0.640906	0.184327	–0.408507
10069	0.632712	–0.929740	*0.0112369*	0.306524	0.597834
10314	0.852834	–0.876093	0.743215	0.488341	0.722034
10365	0.935595	0.287001	0.819802	0.881310	0.878655
10375	0.931178	0.922339	0.844073	0.873755	0.857481
10484	–0.313351	0.349435	*–0.160549*	–0.328447	*–0.0410585*
10486	–0.672011	0.854878	*–0.090105*	*–0.016698*	–0.761538
10488	0.878093	0.818582	*0.134113*	0.622165	0.737795
10649	*–0.0758686*	0.327142	0.856797	0.779665	0.724150
10652	*0.0740217*	–0.798858	–0.338099	0.384259	0.366407
10656	0.940988	–0.911510	–0.483744	0.497887	0.805162
10696	0.676661	0.566986	0.627194	0.740072	0.699345
10720	*0.119794*	0.705416	*0.143122*	0.510573	*0.0138894*
10786	0.511783	*–0.0479686*	–0.302441	*–0.150897*	*–0.145709*
10808	*–0.155534*	0.709710	0.255308	0.386813	–0.326068
10930	0.433592	–0.562770	–0.276616	*0.0991944*	–0.268774

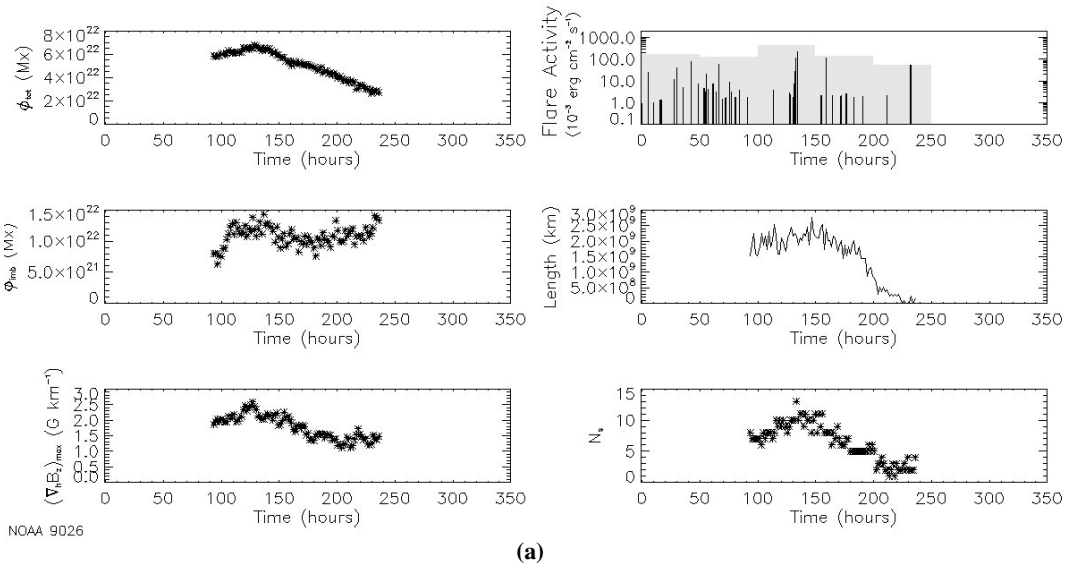

(a)

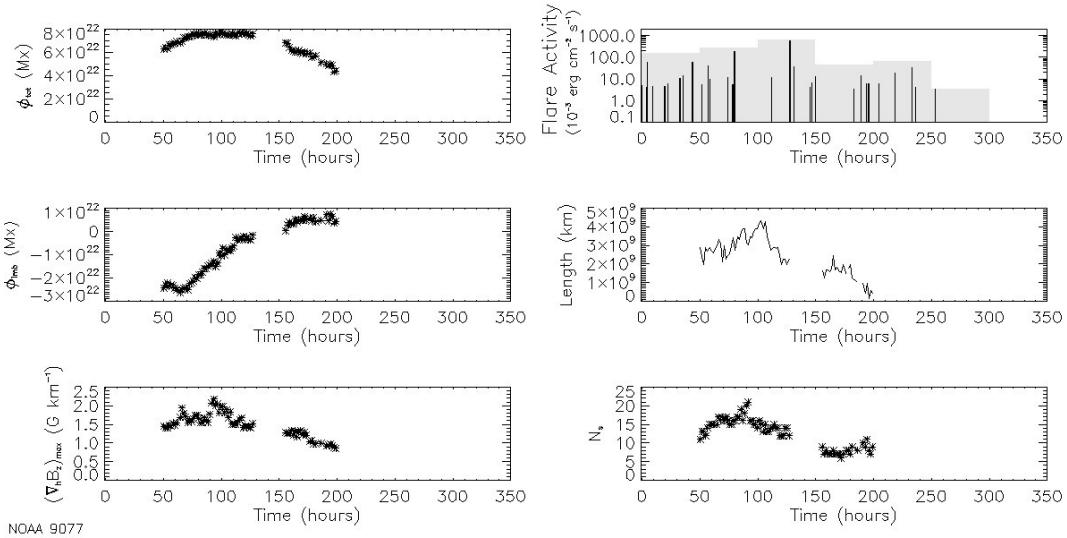

(b)

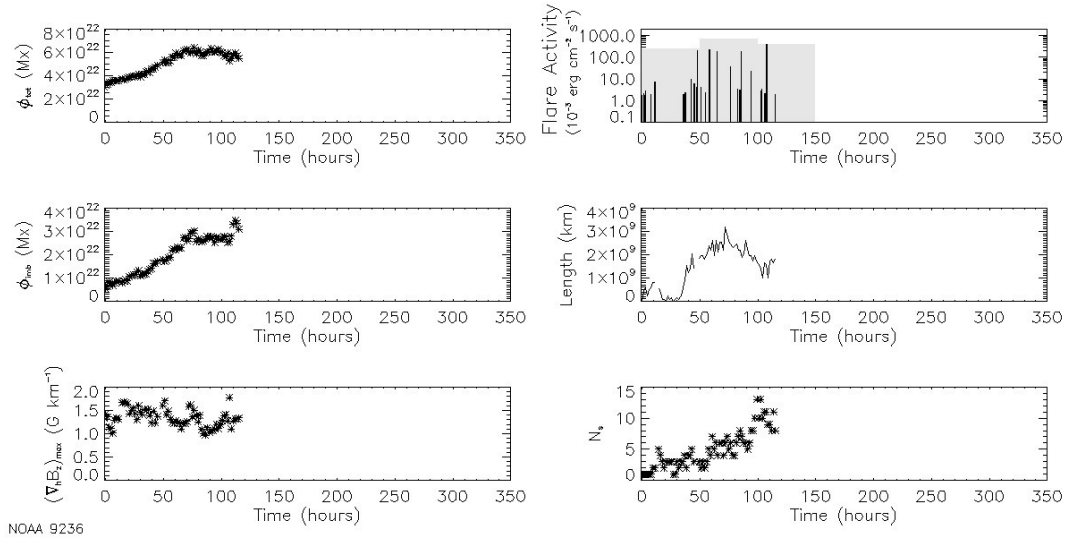

(c)

Fig. B.1. Φ_{tot}, flare activity, Φ_{imb}, l, $(\nabla_h B_z)_{max}$ and N_s vs. time for **a)** NOAA 9026, **b)** 9077 and **c)** 9236.

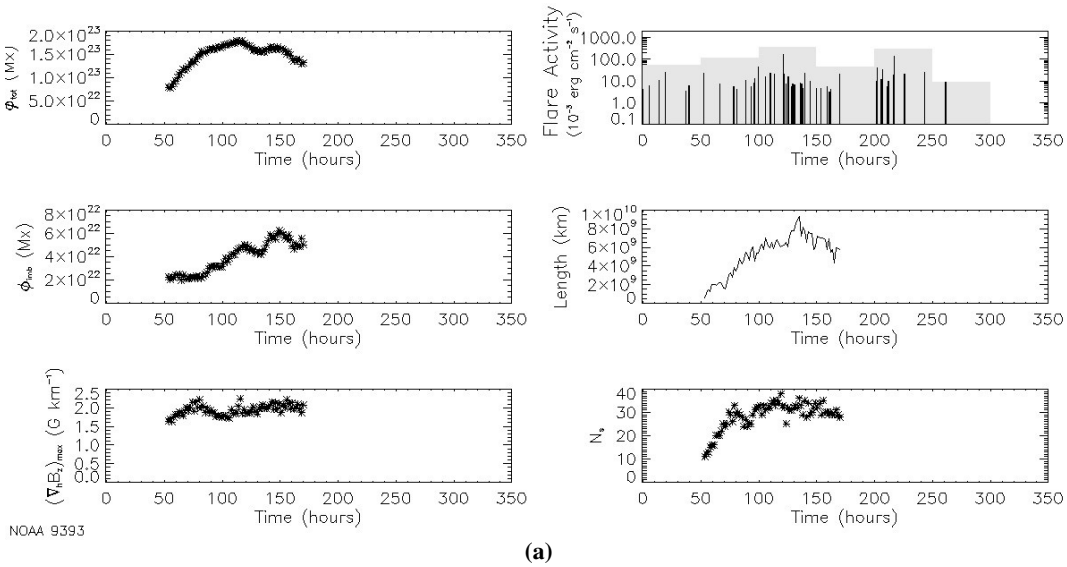

(a)

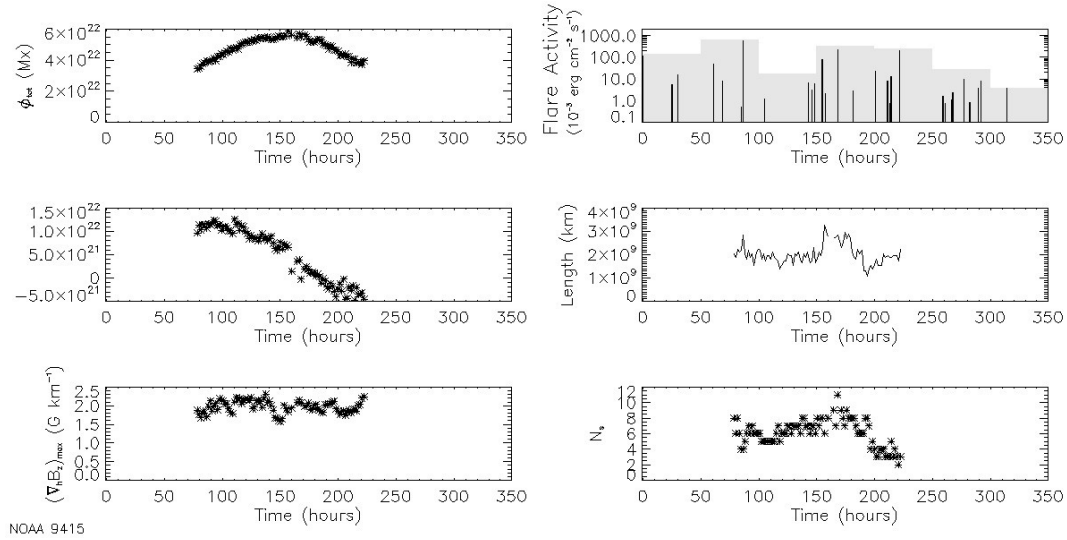

(b)

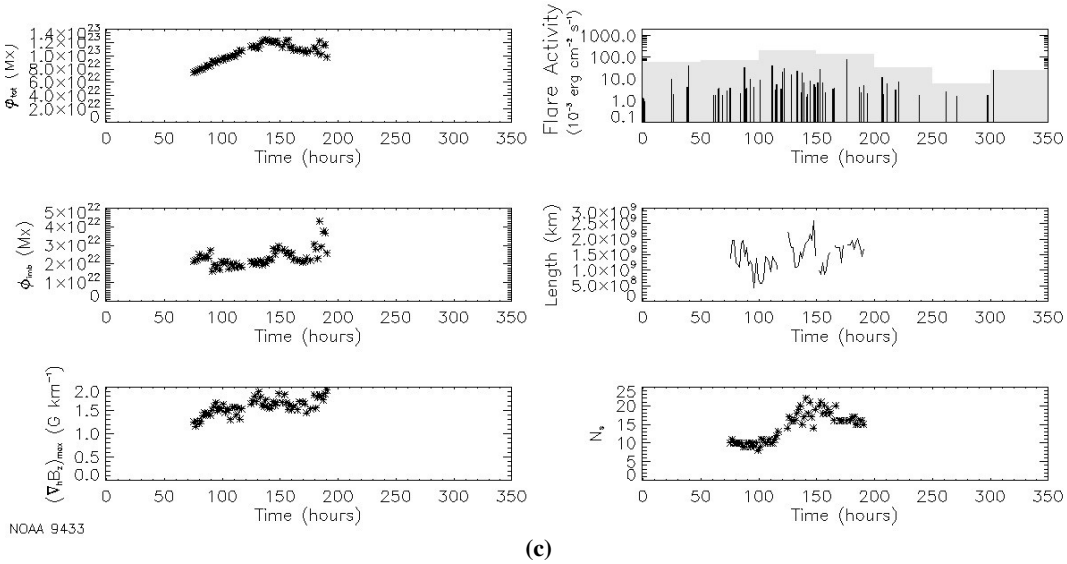

(c)

Fig. B.2. $\Phi_{\rm tot}$, flare activity, $\Phi_{\rm imb}$, l, $(\nabla_{\rm h}B_z)_{\rm max}$ and $N_{\rm s}$ vs. time for **a)** NOAA 9393, **b)** 9415 and **c)** 9433.

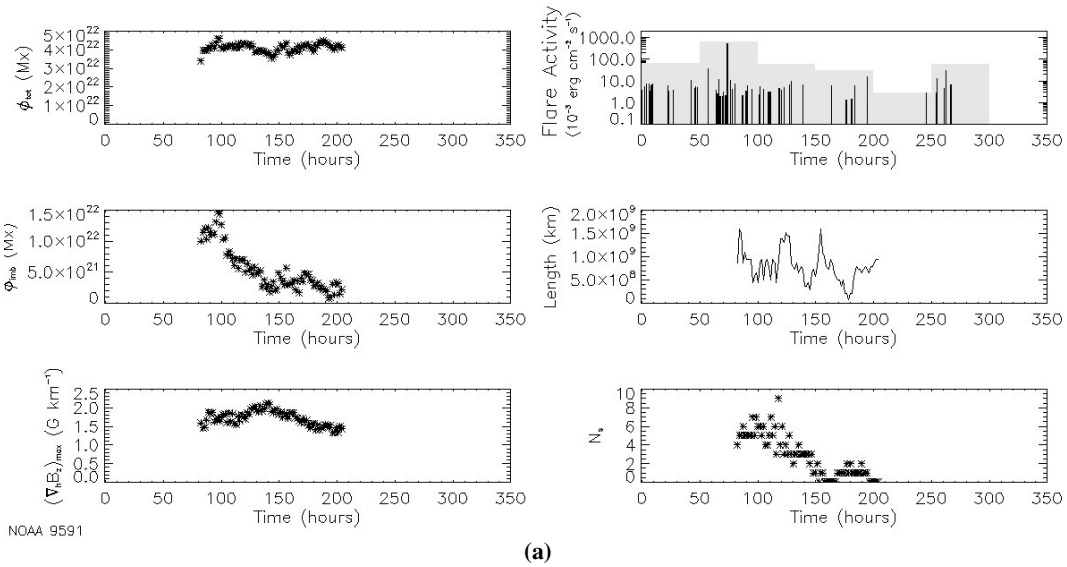

(a)

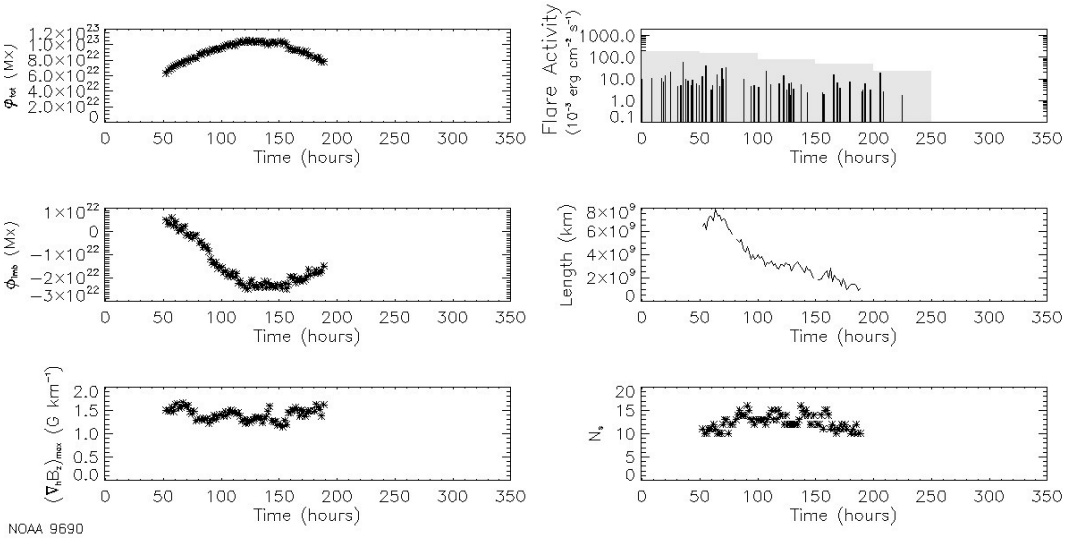

(b)

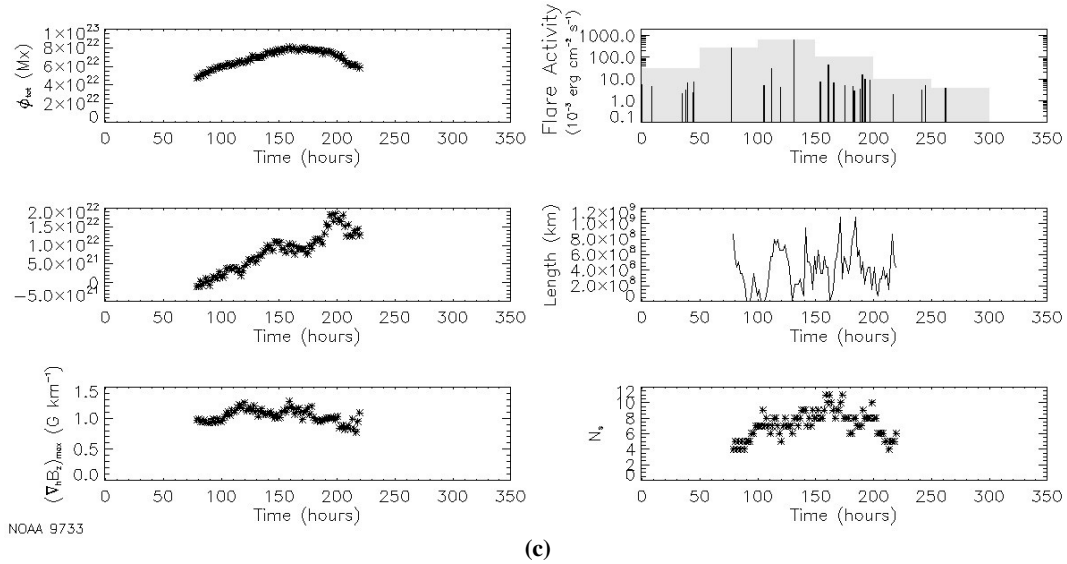

(c)

Fig. B.3. $\Phi_{\rm tot}$, flare activity, $\Phi_{\rm imb}$, l, $(\nabla_{\rm h} B_z)_{\rm max}$ and $N_{\rm s}$ vs. time for **a)** NOAA 9591, **b)** 9690 and **c)** 9733.

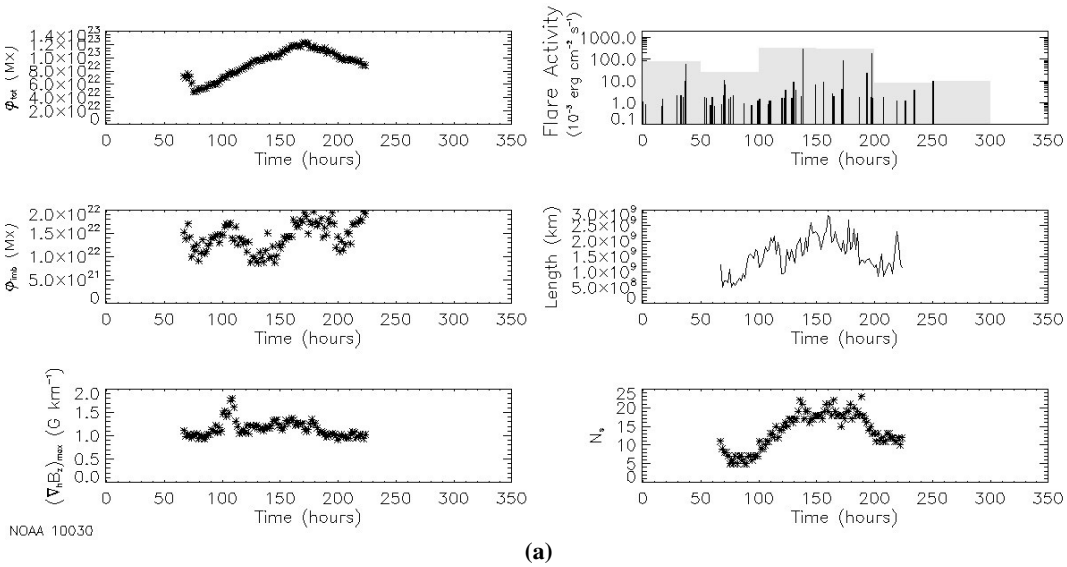

(a)

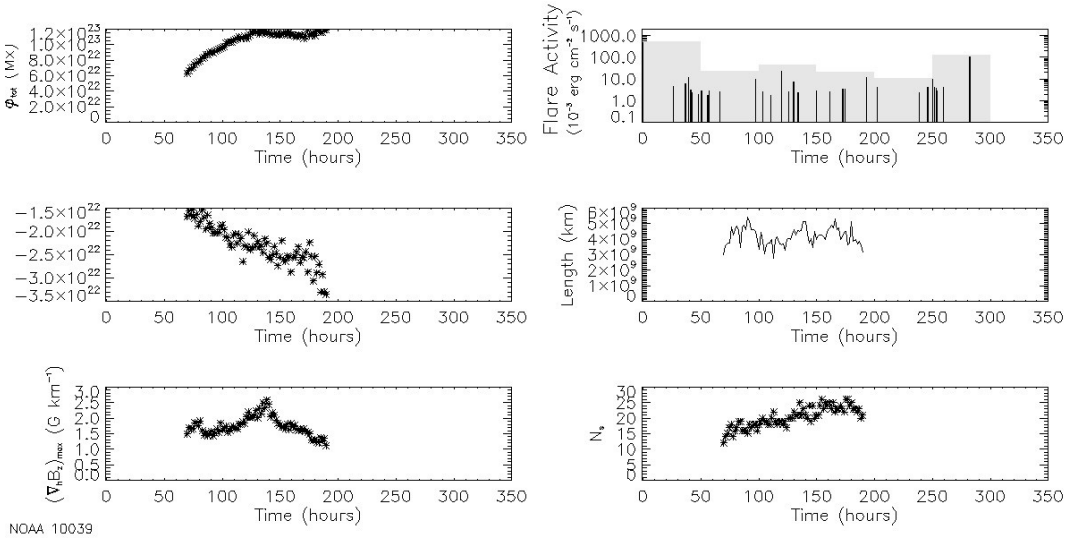

(b)

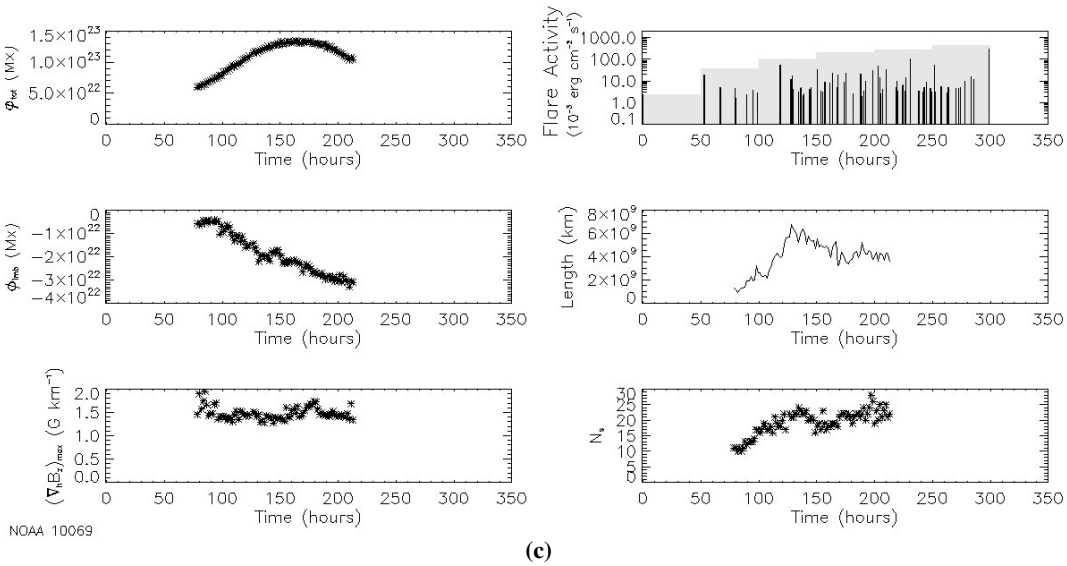

(c)

Fig. B.4. $\Phi_{\rm tot}$, flare activity, $\Phi_{\rm imb}$, l, $(\nabla_{\rm h}B_z)_{\rm max}$ and $N_{\rm s}$ vs. time for **a)** NOAA 10030, **b)** 10039 and **c)** 10069.

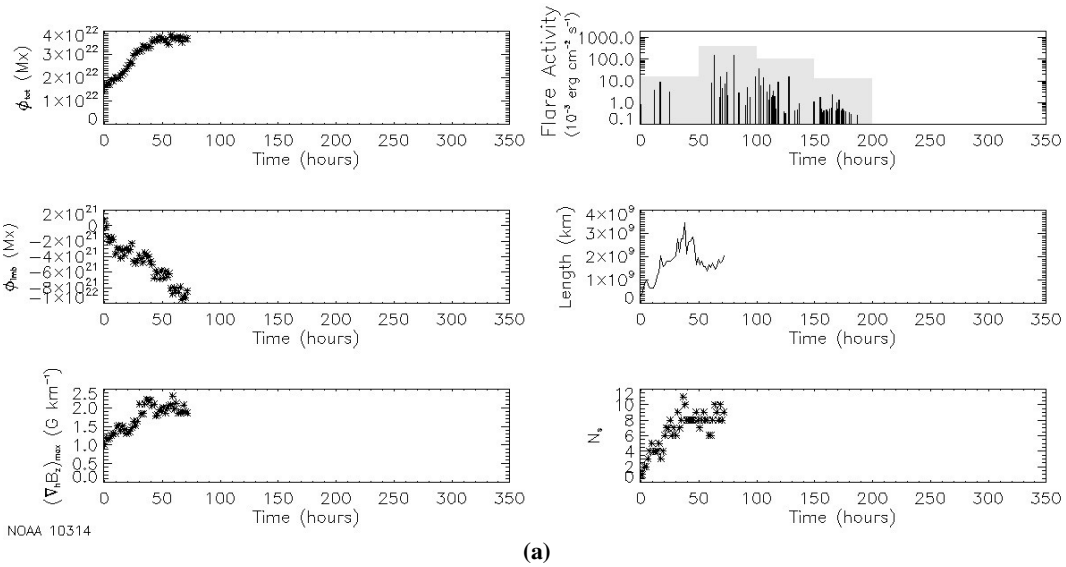

(a)

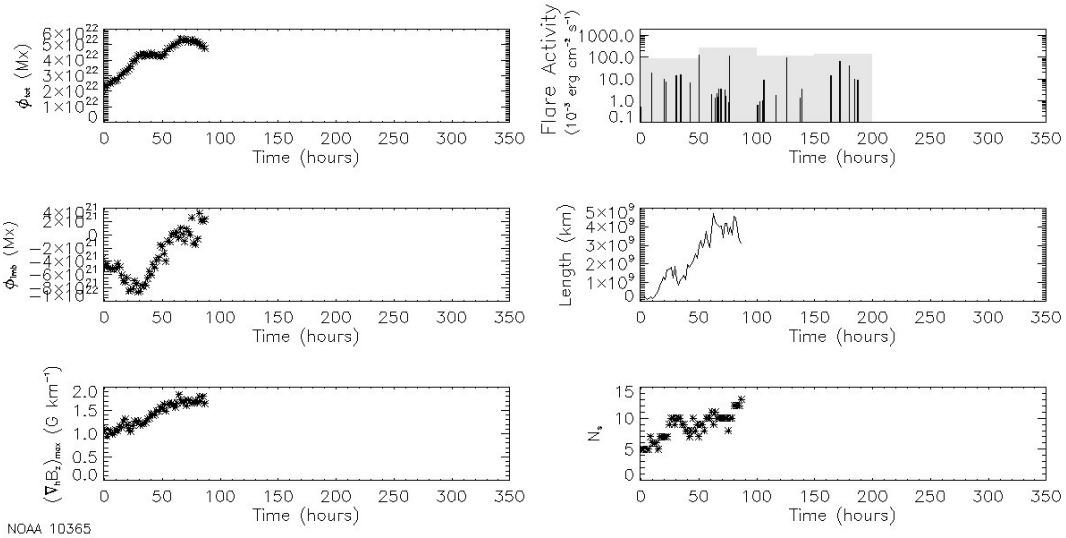

(b)

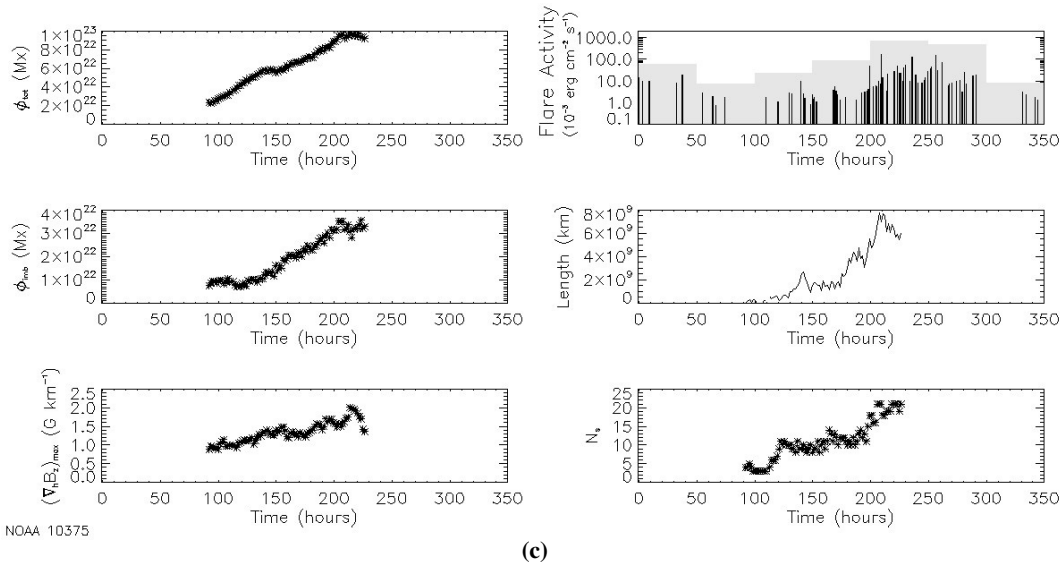

(c)

Fig. B.5. $\Phi_{\rm tot}$, flare activity, $\Phi_{\rm imb}$, l, $(\nabla_{\rm h} B_z)_{\rm max}$ and $N_{\rm s}$ vs. time for **a)** NOAA 10314, **b)** 10365 and **c)** 10375.

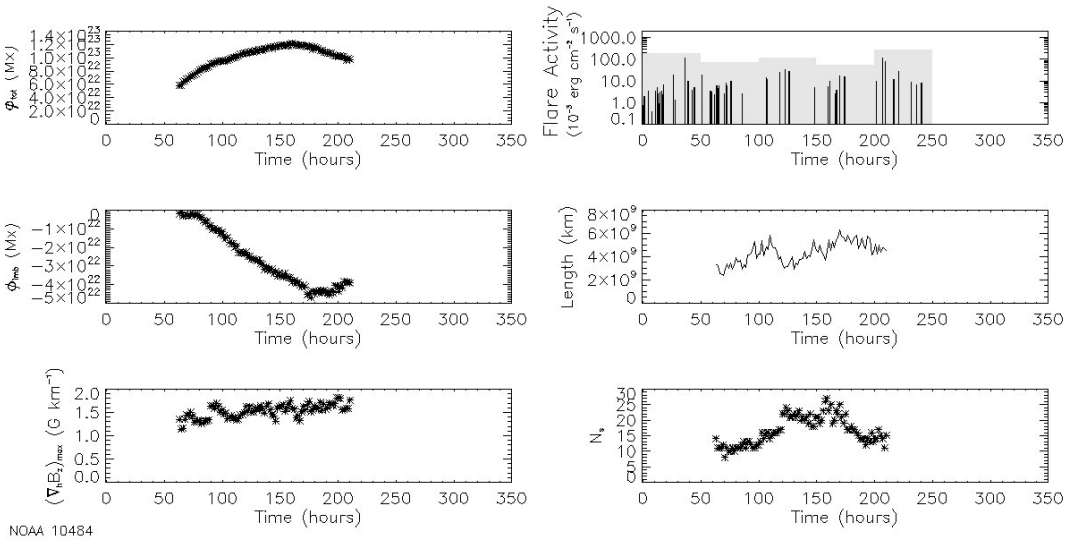

(a)

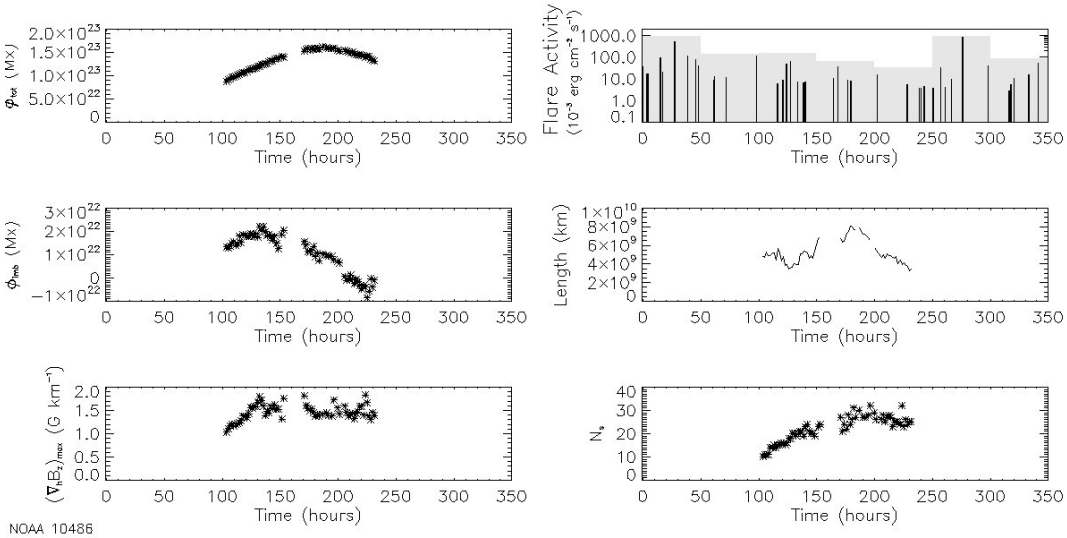

(b)

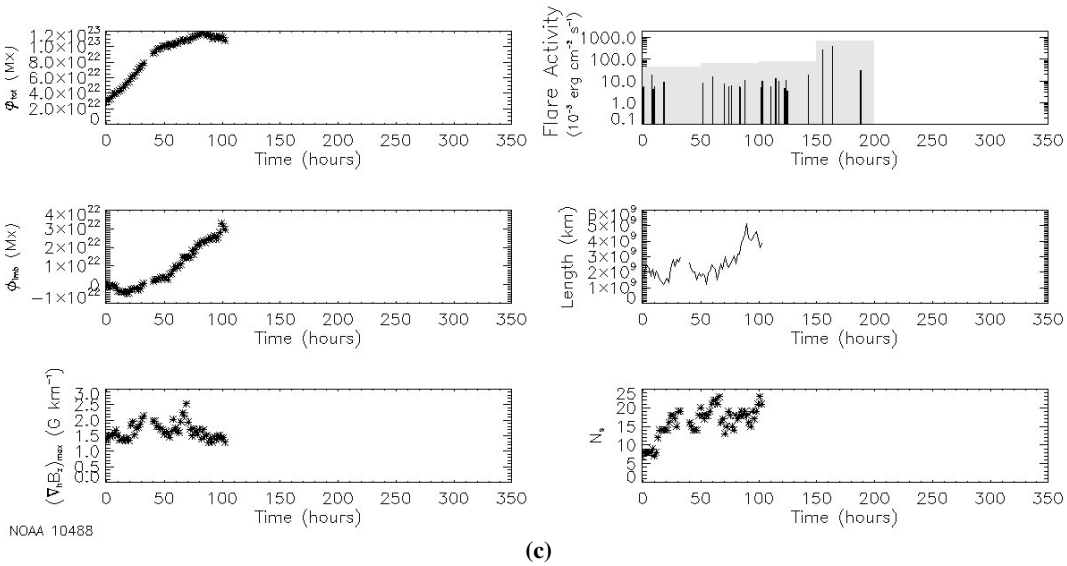

(c)

Fig. B.6. $\Phi_{\rm tot}$, flare activity, $\Phi_{\rm imb}$, l, $(\nabla_{\rm h} B_z)_{\rm max}$ and $N_{\rm s}$ vs. time for **a)** NOAA 10484, **b)** 10486 and **c)** 10488.

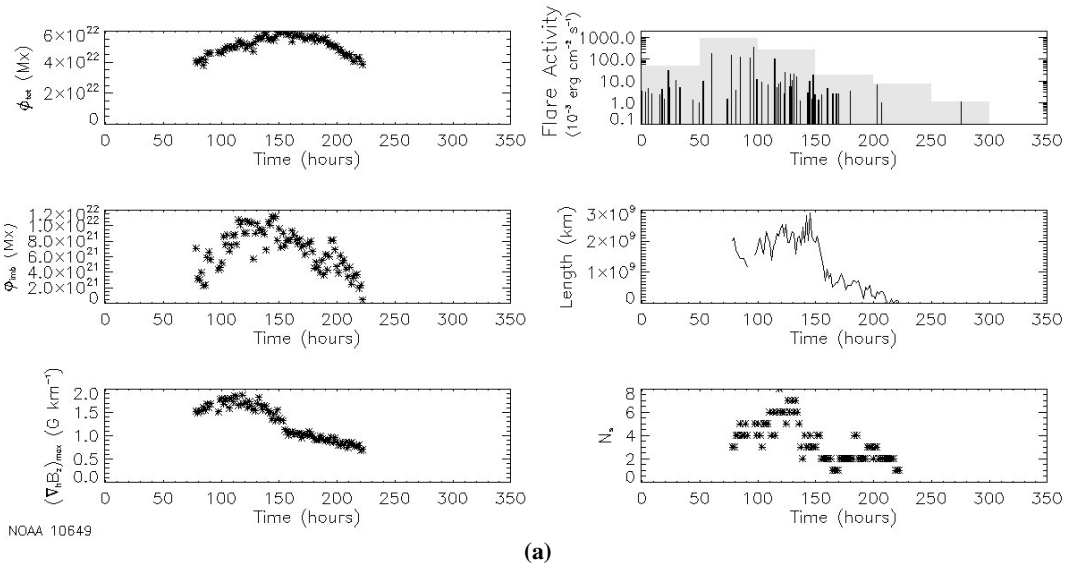

(a)

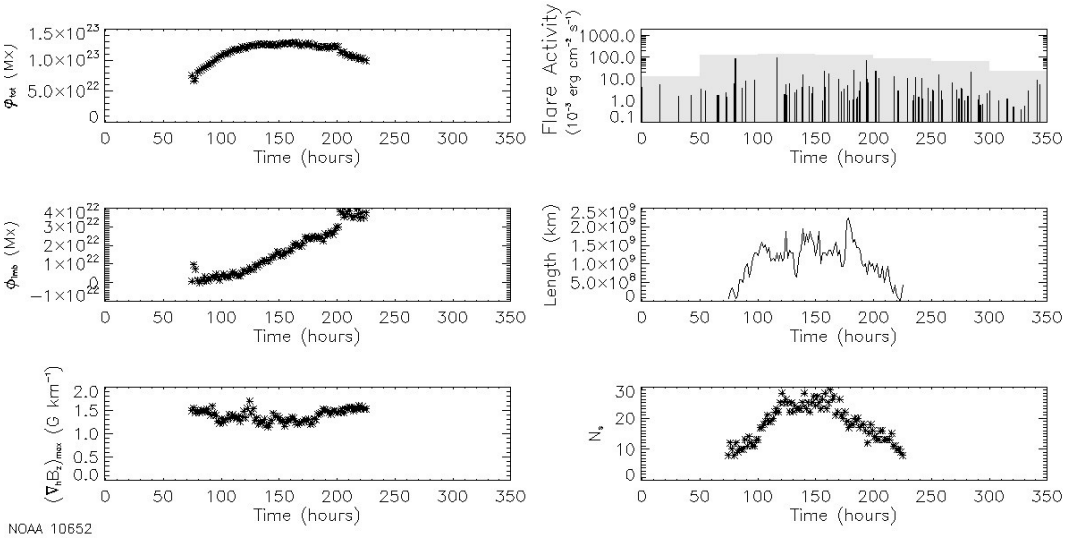

(b)

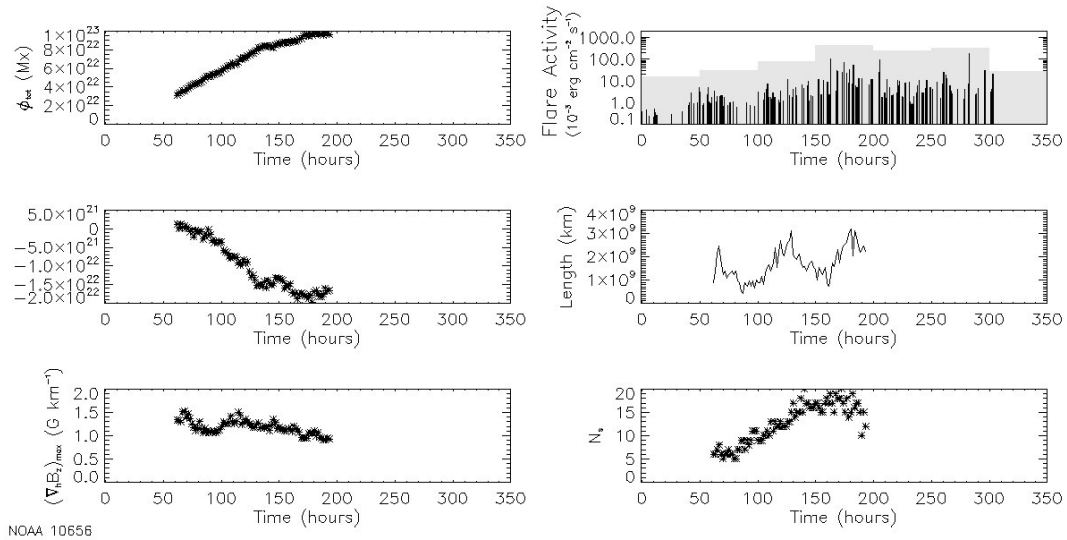

(c)

Fig. B.7. $\Phi_{\rm tot}$, flare activity, $\Phi_{\rm imb}$, l, $(\nabla_{\rm h} B_z)_{\rm max}$ and $N_{\rm s}$ vs. time for **a)** NOAA 10649, **b)** 10652 and **c)** 10656.

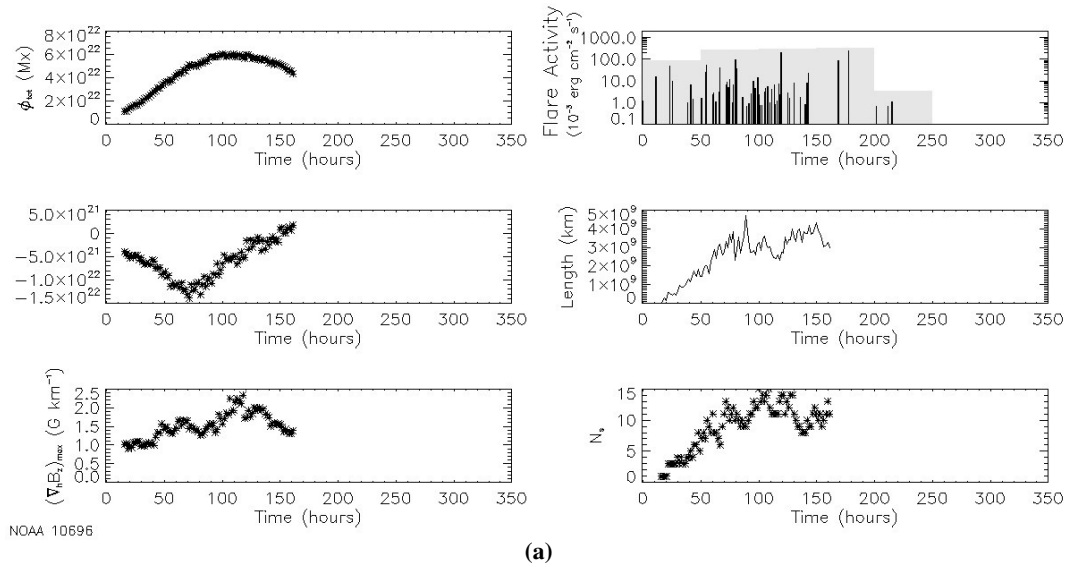

(a)

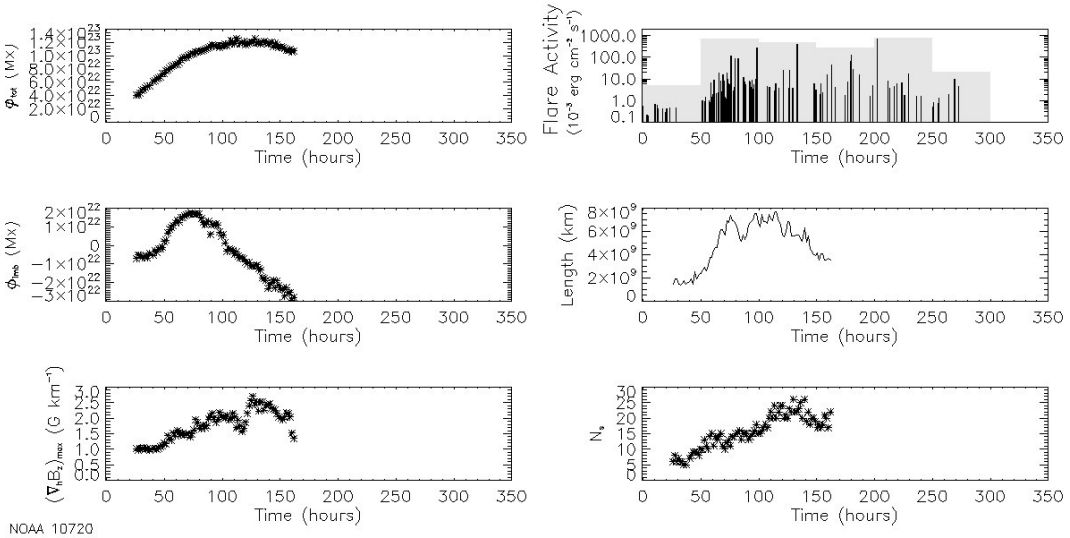

(b)

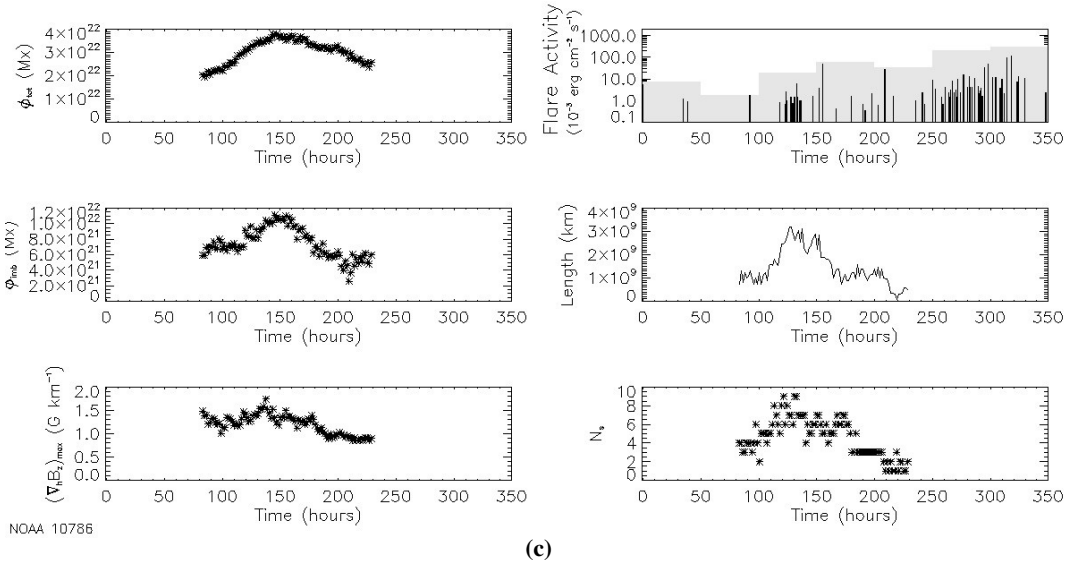

(c)

Fig. B.8. $\Phi_{\rm tot}$, flare activity, $\Phi_{\rm imb}$, l, $(\nabla_{\rm h} B_z)_{\rm max}$ and $N_{\rm s}$ vs. time for **a)** NOAA 10696, **b)** 10720 and **c)** 10786.

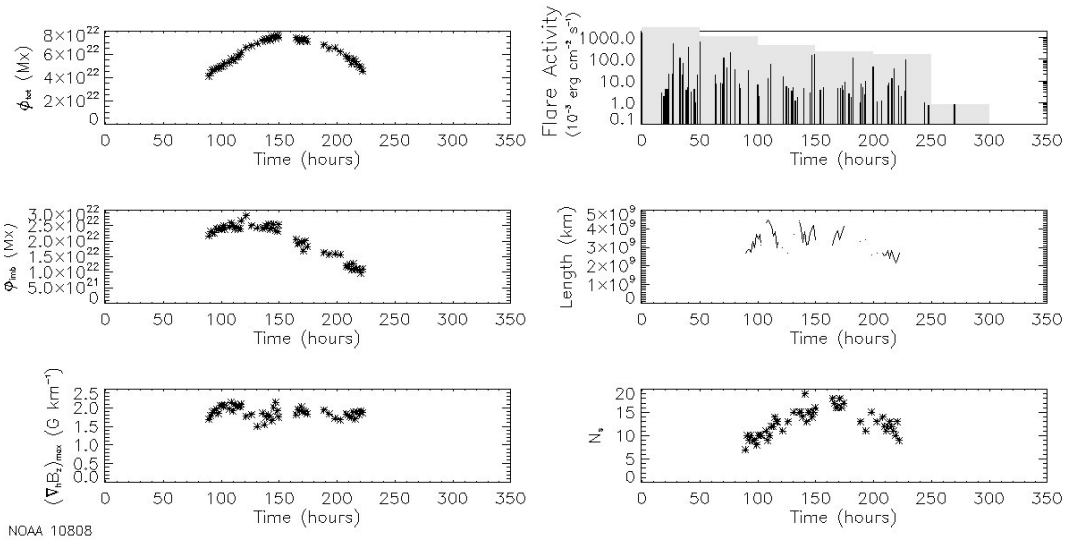

(a)

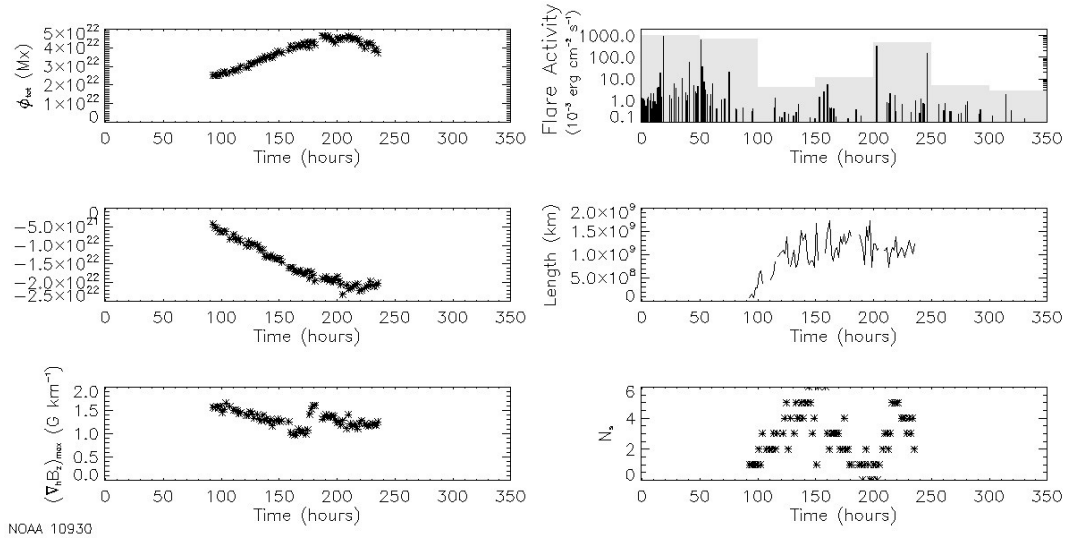

(b)

Fig. B.9. $\Phi_{\rm tot}$, flare activity, $\Phi_{\rm imb}$, l, $(\nabla_{\rm h} B_z)_{\rm max}$ and $N_{\rm s}$ vs. time for **a)** NOAA 10808 and **b)** 10930.